Supplementary Information (SI) for Nanoscale.
This journal is © The Royal Society of Chemistry 2026

Influence of Composition-Phase Interplay on Electrochemical Activity of Ternary Transition Metal Dichalcogenides

*Manoj Palabathuni, Niraj Nitish Patil, Suvodeep.Sen, Geetu Kumari, Sarah Guerin, Shalini Singh**

Email : shalini.singh@ul.ie

Experimental Section

Chemicals : Niobium chloride ($NbCl_5$, 99.9%), Tungsten hexacarbonyl **(**$W(CO)_6$, 99.9%), Sulfur powder (S, 99.9%), Oleylamine (OLA, 70%), Toluene (Tol), Isopropanol (IPA) were purchased from Lennox, Ireland. OLA was purified at 120^0C and stored in glovebox before using for reactions. Rest of the chemicals were used as received without any further purifications.

Synthesis of $Nb_xW_{1-x}S_2$ nanosheets

All the chemicals used are purchased from sigma Aldrich. The $Nb_xW_{1-x}S_2$ nanosheets were prepared by using a hot injection colloidal synthetic route. Whole reaction procedure is processed in Schlenk line under the Ar flow.

Start with 7 ml of oleylamine (OAm) in a three necked round bottomed flask was degassed at 120°C for 30 mins, then the temperature is raised to 300°C. Thereafter, in a vial 1.0 mmol of $W(CO)_6$ and $NbCl_5$ were dissolved in 2 ml of OAm, the mixture was kept at 120°C for 30 min. In the same way, 2 mmol of S is dissolved in 2 ml of OAm in a separate vial, the solution was

heated at 80^{o}C for 30 min. Once the mixtures are properly dissolved, metal and chalcogen mixture are mixed and injected into RB at 320^{o}C with a rate of 0.5 mL min^{-1}. The reaction temperature was maintained at 320^{o}C throughout the reaction time (2 hr). Further allowed to cool down to room temperature by removing heating mantle.

Purification of nanosheets

Washing procedure is fully carried out in glovebox. The synthesized nanosheets are poured in 50 ml centrifuge tube then added 8 ml of toluene and vortexed well and centrifuged at 5000 rpm for 5 min. The pellet was collected and further dispersed in 10 ml of toluene and 10 ml of isopropanol then vortexed and sonicated to disperse and centrifuged another 2 times and dried under vacuum for overnight.

Instrumentation

Electron Microscopy. For TEM analysis, the NCs were dispersed in hexane and drop-cast on continuous carboncoated 300 mesh copper grids. Low-resolution and high-resolution TEM (HRTEM) was conducted by using 200 kV Talos F200i field-emission microscope equipped with a Gatan UltraScan CCD camera and EDAX Genesis energy dispersive X-ray spectroscopy (EDS) detector and Thermo-Fisher Scientific FEI double-aberration-corrected monochromatic Titan Themis with a double tilt holder was used for aberration-corrected TEM and scanning transmission electron microscopy analysis. For analyzing the HRTEM data, interplanar distances and particle orientation were determined from the selected area FFT analysis using GMS3 software.

X-ray diffraction (XRD) analysis. XRD of drop-cast films of the NCs on the flat surface of p-type boron doped silicon zero background was conducted using a PANalytical Empyrean instrument equipped with a Cu Kα radiation source (λ =1.5418 Å) and a 1-D X'celerator strip detector with the diffractometer operating at 40 kV and 40 mA.

X-ray photoelectron spectroscopy (XPS). XPS analysis was conducted using a Kratos AXIS ULTRA spectrometer equipped with a monochromatic Al Kα (1486.58 eV) X-ray source. Calibration was carried out based on the C 1s peak at 284.8 eV. Data processing, including spectrum construction and peak fitting, was completed using Casa XPS software. The XPS measurements were performed on vacuum-dried nanostructure samples to ensure accuracy and consistency in the analysis.

Scanning electron microscopy. Morphology and elemental analysis of the particles examined by field-emission scanning electron microscopy (SEM) on an Auriga Zeiss operated at 5.0 keV.

Electrochemical measurement. All the Electrochemical measurements were conducted at room temperature using an electrochemical workstation with a standard three-electrode setup in a 0.5 M H2SO4 solution. The as-prepared $Nb_XW_{1-X}S_2$ nanosheets served as the working electrodes, with an Ag/AgCl electrode as the reference and a Pt wire as the counter electrode. All measured potentials were converted to the reversible hydrogen electrode (RHE) using the equation E(RHE) = E(Ag/AgCl) + 0.059pH + 0.197. Linear sweep voltammetry (LSV) was performed within a potential range of 0 to -0.8 V vs RHE at a scan rate of 2 mV s^{-1} for the HER. Tafel plots were generated using the Tafel equation ($\eta = a + b \log j$), where j represents current density, b is the Tafel slope, and a is the intercept. Electrochemical impedance spectroscopy (EIS) measurements were taken across a frequency range of 100 kHz to 0.1 Hz, with an AC voltage amplitude of 10 mV. Catalyst durability was assessed via chronoamperometry at a fixed bias over 100 hours.

Nanosheets measurements. The dimensions were measured using ImageJ by drawing a line across the lateral dimension (diameter/edge-to-edge distance) of each nanosheet in the microscopy image. For less well-defined nanosheets, the longest visible lateral dimension was used as an approximate size measure.

Working Electrode preparation.

≈5 mg of the nanosheet catalyst and 1 mg of carbon black was homogeneously dispersed in 500 µl of IPA, 50 µl of distilled water, and 20 µl of 5 wt% Nafion (binder) by 60 min ultrasonication forming casting ink. 5 µl of this prepared ink is drop-casted on the prepolished glassy carbon electrode to coat a 0.62 mg cm^{-2} active catalyst layer.

Table S1.Concentration of Nb and S vacancies in all the compositions confirmed by SEM, TEM and ICP-OES.

$Nb_xW_{1-x}S_2$	Stoichiometric ratios					
	Nb			S		
	XPS	SEM EDX	ICP-OES	XPS	SEM EDX	Avg. S Vacancies
0 (WS2)	0	0	0	2.12	2.07	2.09
0.1	0.10	0.15	0.11	2.02	1.87	1.94
0.3	0.32	0.31	0.34	1.86	1.84	1.85
0.5	0.58	0.60	0.55	1.93	1.83	1.88
0.7	0.68	0.74	0.75	1.91	1.87	1.89
0.9	0.84	0.91	0.89	1.63	1.67	1.65

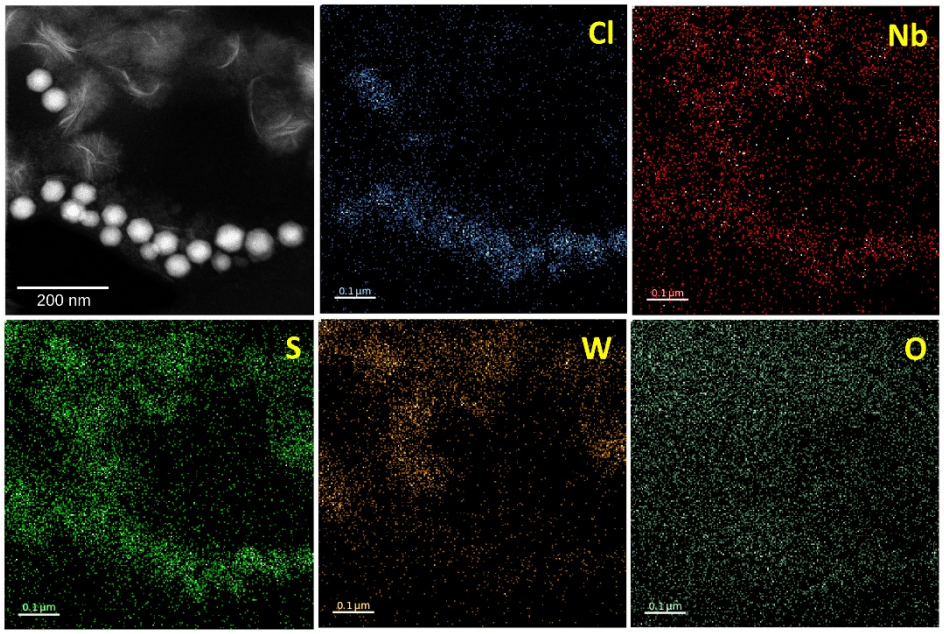

Figure S1. STEM image and elemental mapping of $Nb_xW_{1-x}S_2$ composition with oxide by-products.

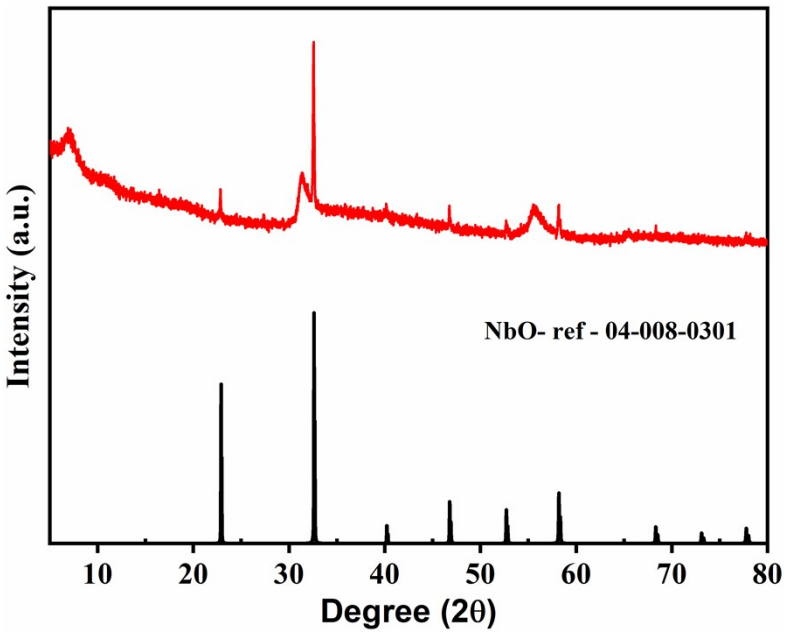

Figure S2. X-ray diffraction of as synthesized $Nb_{0.5}W_{1-0.5}S_2$ using WCl_6 as W source.

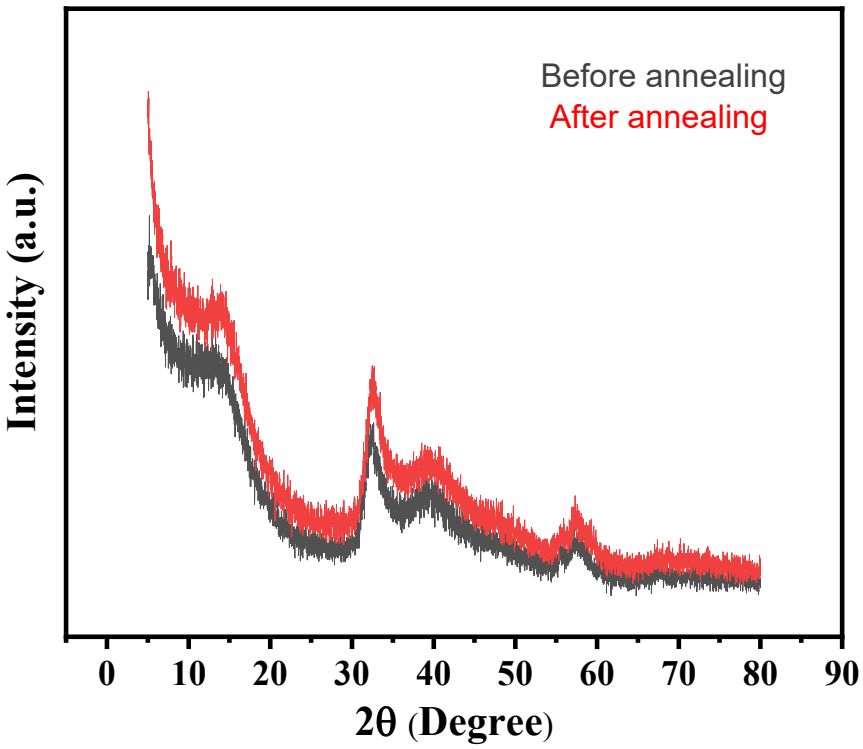

Figure S3. XRD of $Nb_{0.5}W_{1-0.5}S_2$ before and after annealing at 400^0C in Ar.

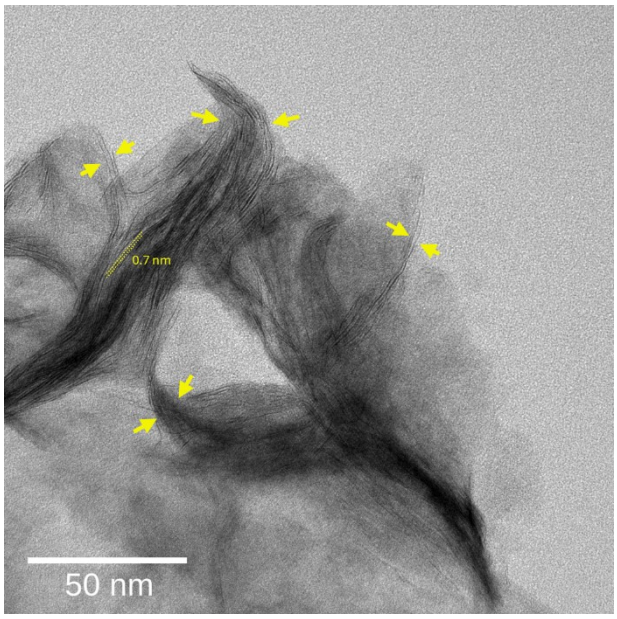

Figure S4. TEM image of $Nb_{0.5}W_{1-0.5}S_2$ nanosheets, highlighted interlayer spacing.

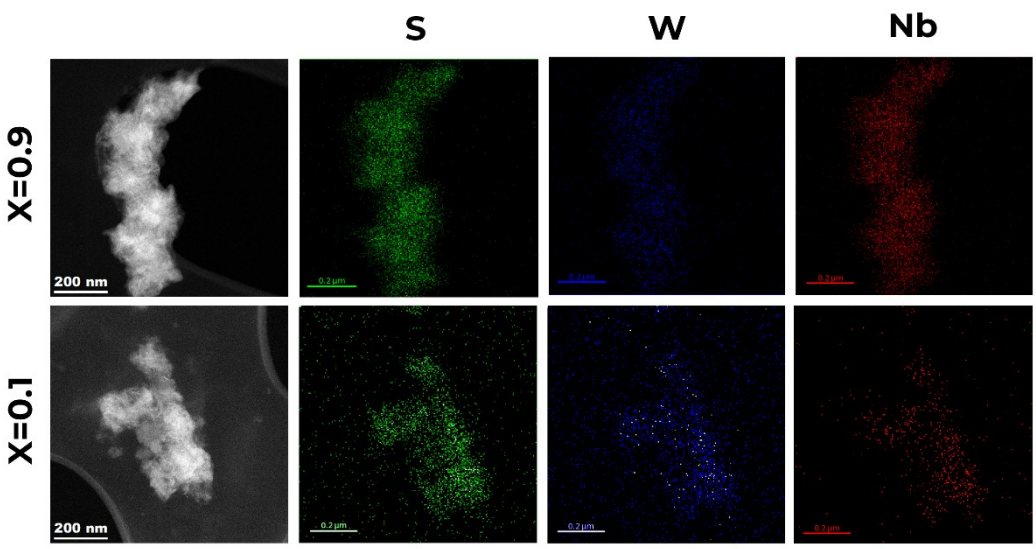

Figure S5. STEM elemental mapping of $Nb_xW_{1-x}S_2$ (x = 0.1&0.9).

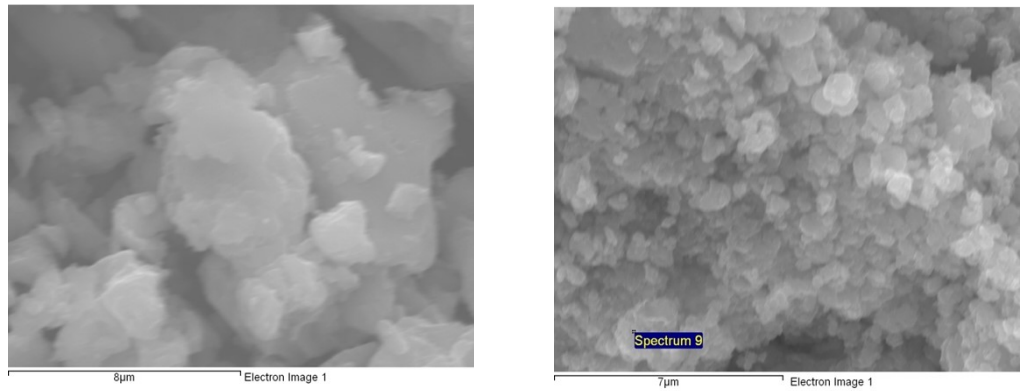

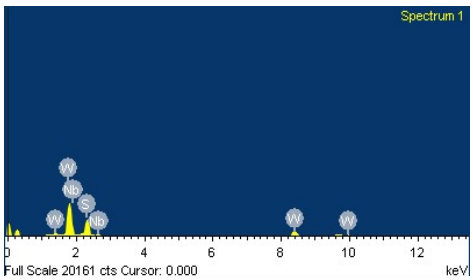

Element	Weight%	Atomic%
S K	34.10	65.20
Nb L	39.28	25.92
W M	26.62	8.88
Totals	100.00	

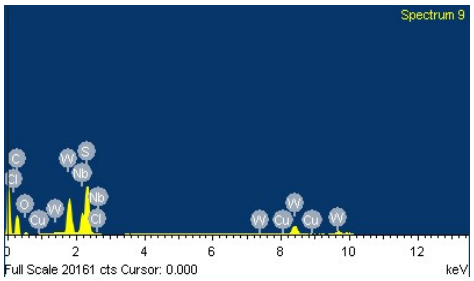

Element	Weight%	Atomic%
S K	30.51	63.80
Nb L	30.44	21.97
W M	39.05	14.24
Totals	100.00	

Figure S6. SEM – EDS spectrum of $Nb_{0.1}W_{1-0.1}S_2$ (left) and $Nb_{0.5}W_{1-0.5}S_2$ (right).

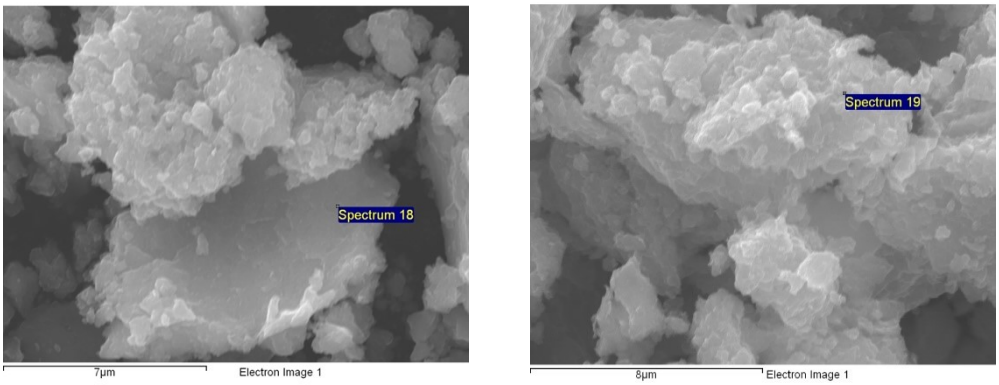

Element	Weight%	Atomic%
S K	26.11	65.17
Nb L	6.25	5.38
W M	67.64	29.44
Totals	100.00	

Element	Weight%	Atomic%
S K	34.84	62.67
Nb L	55.00	34.14
W M	10.17	3.19
Totals	100.00	

Figure S7. SEM – EDS spectrum of $Nb_{0.7}W_{1-0.7}S_2$ (left) and $Nb_{0.9}W_{1-0.9}S_2$ (right).

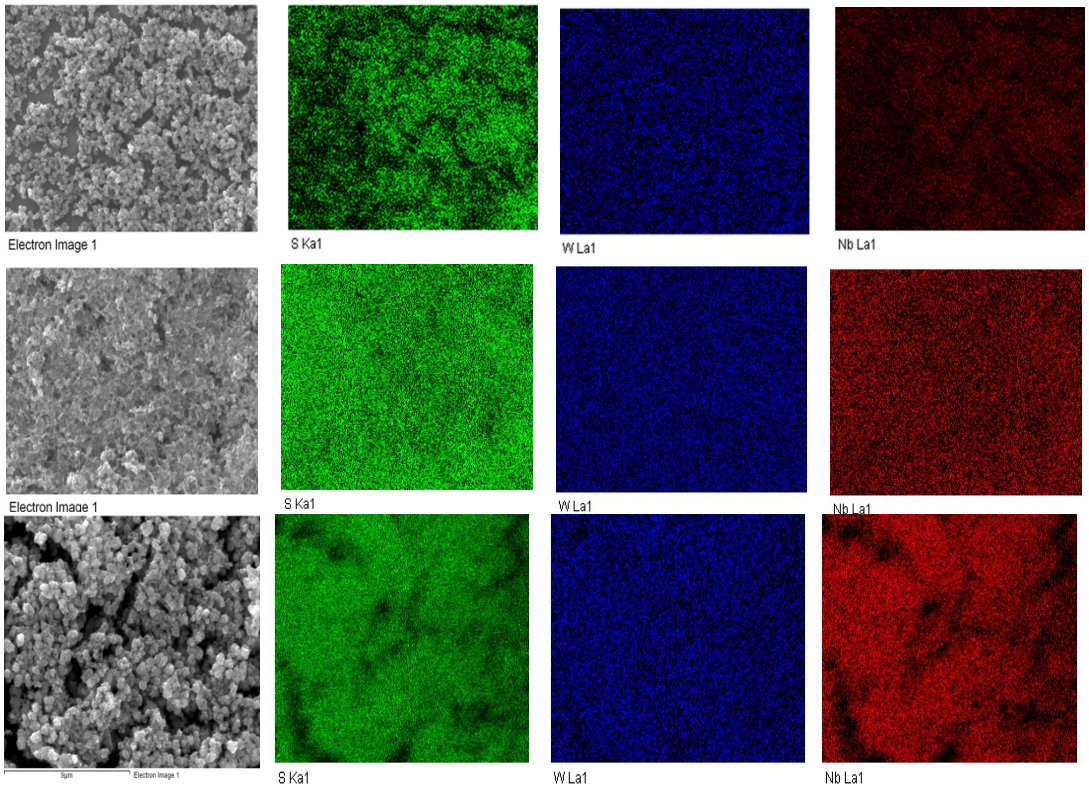

Figure S8. SEM – EDX mapping of $Nb_xW_{1-x}S_2$ (x = 0.1, 0.5 & 0.9).

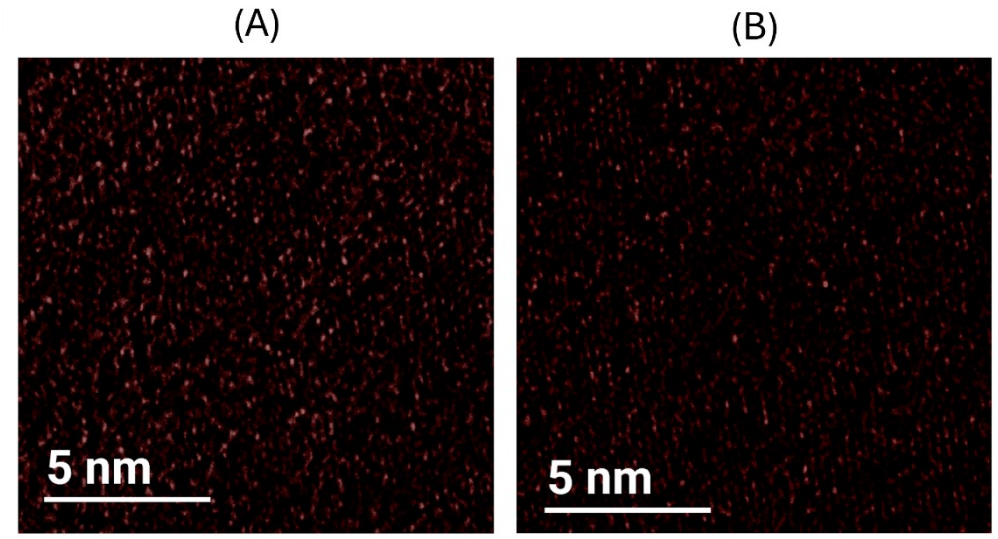

Figure S9. Contrasted HRTEM of $Nb_xW_{1-x}S_2$ (x = 0.3&0.5).

Table S2. Yield of all the $Nb_xW_{1-x}S_2$ compositions.

Nb fraction	Composition	Theoretical weight (mg)	Yield weight	Yield (%)
0.1	$Nb_{0.1}W_{0.9}S_2$	119	90	75.6
0.3	$Nb_{0.3}W_{0.7}S_2$	110	92	83.6
0.5	$Nb_{0.5}W_{0.5}S_2$	101	83	82.2
0.7	$Nb_{0.7}W_{0.3}S_2$	92	80	87
0.9	$Nb_{0.9}W_{0.1}S_2$	83	73	88

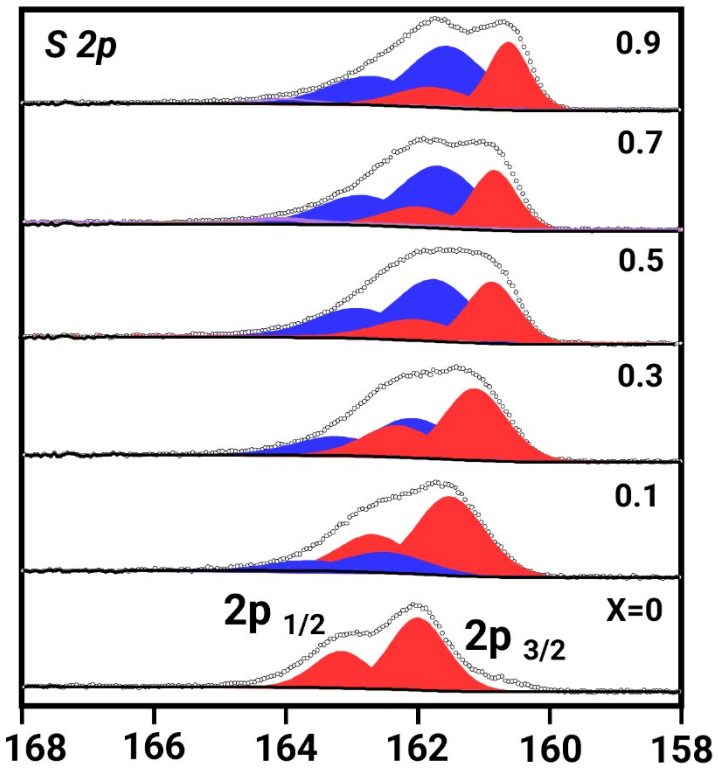

Figure S10. XPS - sulfur 2p spectra of (x = 0 to 0.9) $Nb_xW_{1-x}S_2$.

The assigned peaks for sulfur, S 2p3/2 and 2p1/2 peaks appears at 162 and 163.17 eV respectively, with splitting of 1.17 eV, this represents a redshift of 2.2 eV compared to neutral S (S^0) peaks at 164.2 and 165.2 eV. The peaks in X=0 correspond (assigned to S1) to the S^{2-} anion bonded to the cation (W) in WS_2 in 2H phase.[6] In case of X≥0.1 it resolved in to four bands, two corresponds (S1 band) to S binding with the W^{4+}/Nb^{4+} and the remaining two binding (S2 band) with the Nb^{3+}. The S2 band becomes more significant with increase in x, from the increased contribution of Nb^{3+}.

Table S3. HER performance comparison with previous reports.

Compositions	**Overpotential**	**Tafel slope (*b*)**	**Ref**
$Nb_xW_{1-x}S_2$	190	120	Current work
WS_2-Nb	–	167	1
WS_2-Ta	–	–	
WSSe-rGO	285	98	2
WS_2-WO_3	305	134	3
WS_2 NFs	351	84	
$W_xMo_{1-x}S_2$-rGO	285	38.7	4
$Nb_xW_{1-x}S_y$ films	222	126	5

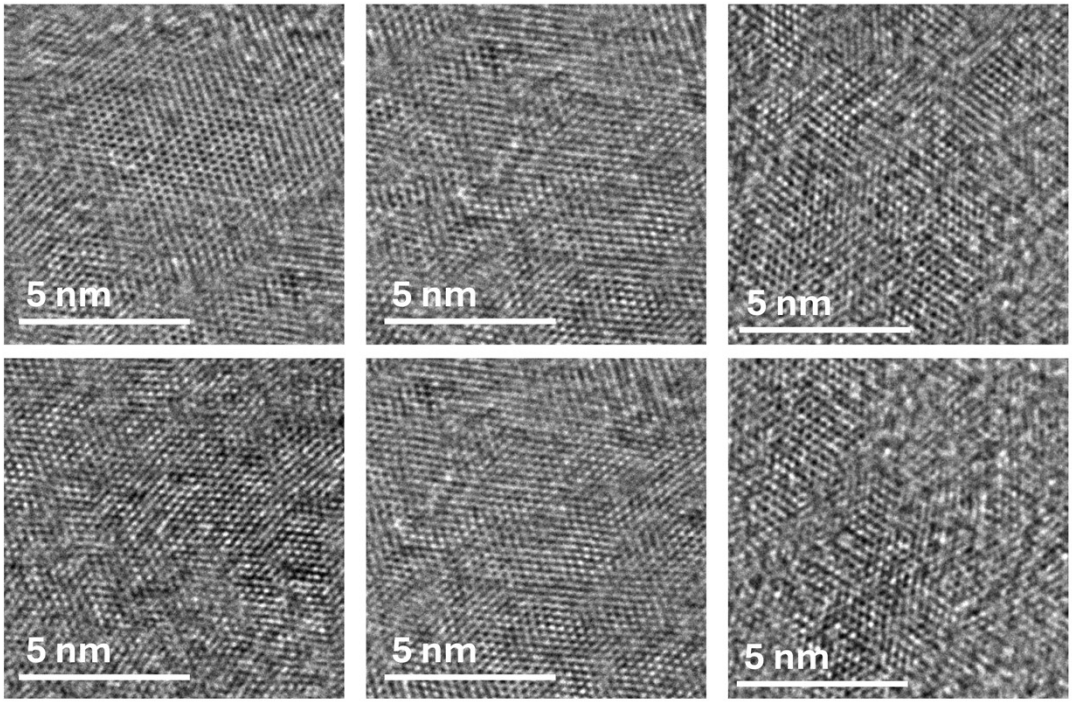

Figure S11. Additional HRTEM of $Nb_xW_{1-x}S_2$ (x = 0.1).

Table S4. 2(θ) values of (100) and (008) planes derived to calculate a and c lattice constants.

Composition (x)	2(θ)	
	(100)	(008)
0	33.08	58.74
0.1	32.25	56.94
0.3	32.46	57.33
0.5	31.66	56.31
0.7	31.96	56.37
0.9	32.36	57.49

REFERENCES

(1) Chua, X. J.; Luxa, J.; Eng, A. Y. S.; Tan, S. M.; Sofer, Z.; Pumera, M. Negative Electrocatalytic Effects of P-Doping Niobium and Tantalum on MoS2 and WS2 for the Hydrogen Evolution Reaction and Oxygen Reduction Reaction. *ACS Catal.* **2016**, *6* (9), 5724–5734. https://doi.org/10.1021/acscatal.6b01593.

(2) Gowrisankar, A.; Sherryn, A. L.; Selvaraju, T. In Situ Integrated 2D Reduced Graphene Oxide Nanosheets with MoSSe for Hydrogen Evolution Reaction and Supercapacitor Application. *Appl. Surf. Sci. Adv.* **2021**, *3*, 100054. https://doi.org/10.1016/j.apsadv.2020.100054.

(3) Nguyen, T. V.; Nguyen, T. P.; Le, Q. V.; Dao, D. V.; Ahn, S. H.; Kim, S. Y. Facile Route for Synthesizing WS2/W2C Nano Hollow Flowers and Their Application for Hydrogen Evolution Reaction. *J. Alloys Compd.* **2023**, *955*, 170231. https://doi.org/10.1016/j.jallcom.2023.170231.

(4) Lei, Y.; Pakhira, S.; Fujisawa, K.; Wang, X.; Iyiola, O. O.; Perea López, N.; Laura Elías, A.; Pulickal Rajukumar, L.; Zhou, C.; Kabius, B.; Alem, N.; Endo, M.; Lv, R.; Mendoza-Cortes, J. L.; Terrones, M. Low-Temperature Synthesis of Heterostructures of Transition Metal Dichalcogenide Alloys (WxMo1–xS2) and Graphene with Superior Catalytic Performance for Hydrogen Evolution. *ACS Nano* **2017**, *11* (5), 5103–5112. https://doi.org/10.1021/acsnano.7b02060.

(5) Schulpen, J. J. P. M.; Lam, C. H. X.; Dawley, R. A.; Li, R.; Jin, L.; Ma, T.; Kessels, W. M. M.; Koester, S. J.; Bol, A. A. Correction to Nb Doping and Alloying of 2D WS2 by Atomic Layer Deposition for 2D Transition Metal Dichalcogenide Transistors and HER Electrocatalysts. *ACS Appl. Nano Mater.* **2024**, *7* (10), 12205–12206. https://doi.org/10.1021/acsanm.4c02304.

(6) Kapuria, N.; Patil, N. N.; Sankaran, A.; Laffir, F.; Geaney, H.; Magner, E.; Scanlon, M.; Ryan, K. M.; Singh, S. Engineering Polymorphs in Colloidal Metal Dichalcogenides: Precursor-Mediated Phase Control, Molecular Insights into Crystallisation Kinetics and Promising Electrochemical Activity. *J. Mater. Chem. A* **2023**, *11* (21), 11341–11353. https://doi.org/10.1039/D2TA09892J.